A study of multiple equilibria in a β-plane and a hemispheric model of a barotropic atmosphere

By SYLVIE GRAVEL* and JACQUES DEROME, *Department of Atmospheric and Oceanic Sciences, McGill University, Montréal, Québec, Canada, H3A 2K6*

ABSTRACT

We examine the equilibrium solutions of two topographically forced barotropic models, one having a β-plane geometry and the other being formulated in spherical coordinates. In both models the topography is represented by a single harmonic to facilitate the study of bent resonance, and the flow is forced through a mean zonal wind driving term. The horizontal scale of the topography and the dissipation time scales are selected to yield forced waves of comparable amplitudes in the limit of linear flows. For both models, a steady state version is used to obtain the equilibrium solutions and to derive the linear stability properties of the equilibria. A second, time-dependent nonlinear version of both models is also used to investigate the time evolution of the flow when the equilibrium solutions are perturbed. Our results for the β-plane model indicate that while multiple equilibria can be found for sufficiently low dissipation rates, only one equilibrium is stable and observable over a significant period of time in a time-dependent model. In regions of parameter space where multiple equilibria exist, the unstable equilibrium solutions are not surrounded by limit cycles. Initial states chosen close to these unstable equilibria therefore evolve towards the one stable solution. The spherical geometry model also possesses multiple equilibria for sufficiently low dissipation rates in association with the presence of a bent resonance. Two of the equilibria are stable, one corresponding to a low zonal index flow and the other to a high zonal index flow. The multiple equilibria exist, however, only over a rather narrow range of u^*, the mean zonal wind driving parameter.

1. Introduction

Charney and DeVore (1979), (CD), and Wiin-Nielsen (1979) showed that some simple nonlinear atmospheric models can possess multiple equilibrium solutions in certain parameter regimes. The former authors showed that in the presence of orography and dissipation, the zonally forced barotropic vorticity equation has a stable equilibrium state with a large zonal index, which one could associate with the normal state of the atmosphere, and another stable equilibrium state with a low zonal index, corresponding to "blocked" or anomalous flows. Wiin-Nielsen (1979) used a spherical geometry model with dissipation and an explicit source of vorticity for both the zonal flow

and a wave. He found both stable equilibrium solutions, which he associated with long-lasting atmospheric flows, and an unstable equilibrium solution, which he compared to observed rapidly changing flows.

These introductory papers were followed by many others. Tung and Rosenthal (1985), (TR), published a critical review of the theories of multiple equilibria. Their re-examination covered, in particular, the works of CD, Yoden (1985a), Källén (1982), Legras and Ghil (1985), and with a particular attention, the results of Charney et al. (1981) and Rambaldi and Mo (1984). Charney et al., had extended the model used by CD to include a more realistic representation of the topography. After correcting a minor algebraic error of Charney et al., TR found that the 5 stationary solutions obtained by these authors reduced to three; and furthermore, when the number of degrees of freedom of the system was increased, the number of solutions dropped to one.

---

* Present Affiliation: Division de Recherche en prévision numérique, Service de l'environnement atmosphérique, Dorval, Québec, Canada, H9P 1J3.

In their calculations, Rambaldi and Mo used a longer damping time for their zonal flow U than for the stationary waves. TR found no justification for treating differently the zonal and the other flow quantities. After redoing the calculations with this correction, they found that, indeed, there existed more than one wave solution for each value of U when the damping was weak enough, but the additional solutions were not *equilibrium solutions* in the presence of damping, in the sense that they were unstable to form-drag instability. TR then concluded that with a realistic magnitude of topographic elevation, a physically based zonal driving, Ekman damping, and an adequate spectral representation, multiple equilibria do not exist.

In the present study, we wish to demonstrate the strong dependence of the above mentioned results on the geometry of the model domain. A series of integrations is done for a range of parameter values using a β-plane and a hemispheric model, to compare the emergence and coexistence of solutions along with their stability. For both models a steady-state version is used to find the equilibrium solutions and to determine their stability to weak amplitude disturbances; a time-dependent version is also used to further investigate the stability properties of the equilibrium states when appropriate.

As in the work of Legras and Ghil (1985) and TR, the search of the parameter space for solutions for the 2 models is conducted with the use of a continuation algorithm (Keller, 1978), a technique particularly appropriate to study systems with complex solution diagrams and with periodic solutions.

In the first part of this paper, a description of the barotropic numerical model on the β-plane will be given together with an analysis of the results obtained from applying the continuation algorithm to find the steady-state and periodic solutions. In the second part, the same approach is used with the hemispheric model and a comparison is made between the results of the two models.

2. The β-plane model

2.1. Formulation

The governing equation for the barotropic model is given by the potential vorticity equation

$$\frac{\partial}{\partial t} \nabla^2 \psi + J(\psi, q) = \frac{1}{\tau} \nabla^2 (\psi^* - \psi), \qquad (2.1)$$

where, in the β-plane approximation,

$$q = \nabla^2 \psi + \beta y + \frac{f_0}{H} h \qquad (2.2)$$

is the potential vorticity, h, the topography, ψ^*, the external forcing, H, the atmospheric scale height, τ the dissipation time constant and ∇^2 is the horizontal Laplace operator.

The presence of two rigid walls at the northern and southern boundaries imposes a restriction on the meriodional component of the wind,

$$v = v' = 0 \qquad \text{at} \quad y = 0, D, \qquad (2.3)$$

where v' is the ageostrophic meridional wind component and D represents the width of the channel. Except where noted otherwise, D will be set to 4000 km; the length of the channel is always set to 28000 km, corresponding to the length of the latitude circle at $45°$ N.

In agreement with TR, who found an explicit expression for a zonal momentum forcing u^* in terms of the density weighted vertical integral of zonal mean lateral flux of angular momentum, and no firm physical basis for the presence of a vorticity source in a barotropic model, we use a forcing of the form

$$\psi^* = -u^* y \rightarrow \nabla^2 \psi^* = 0. \qquad (2.4)$$

This implies that the external forcing does not appear explicitly in the vorticity equation. It is therefore necessary to use the zonal momentum equation

$$\frac{\partial u}{\partial t} + u \frac{\partial u}{\partial x} + v \frac{\partial u}{\partial y} - f_0 v' + \beta y v = \frac{1}{\tau} (u^* - u), \qquad (2.5)$$

to see how the presence of the forcing mechanism affects the solutions. In the above, (u, v) are the geostrophic components of the wind and v' the ageostrophic meridional component. When zonally averaged, (2.5) reduces to

$$\frac{\partial \bar{u}}{\partial t} + v \frac{\partial \bar{u}}{\partial y} - \overline{f_0 v'} = \frac{1}{\tau} (\overline{u^*} - \bar{u}), \qquad (2.6)$$

and since v and v' are identically zero at $y = 0$ and D, a stationary solution will exist only if

$$\frac{\partial \bar{u}}{\partial t} = \frac{1}{\tau}(u^* - \bar{u}) \qquad \text{at} \quad y = 0, D. \tag{2.7}$$

This condition is satisfied when the zonal wind $\bar{u}$ is such that

$$\bar{u} = u_0 + u_1(y, t), \qquad u_0 = u^*$$

and $\tag{2.8}$

$$u_1(y = 0) = u_1(y = D) = 0.$$

If the streamfunction is rewritten as the sum of a linearly varying part and a wavy field:

$$\psi = -u^* y + \phi(x, y, t), \tag{2.9}$$

it becomes apparent how in the vorticity equation the wavy part of the streamfunction is affected by the presence of the forcing u^*, since then

$$\frac{\partial}{\partial t} \nabla^2 \phi + J\left(\phi, \nabla^2 \phi + \beta y + \frac{f_0}{H} h\right)$$

$$+ u^* \frac{\partial}{\partial x}\left(\nabla^2 \phi + \frac{f_0}{H} h\right) = \frac{1}{\tau}(-\nabla^2 \phi). \tag{2.10}$$

The wavy part of the steamfunction, ϕ, is then represented using a spectral expansion

$$\phi(x, y, t) = \sum_{i=1}^{L} x_i(t) G_i(x, y), \tag{2.11}$$

where the basis functions G are taken from the set

$$G_i \in \left\{ \sqrt{2} \cos \frac{\pi}{D} ny, \, 2 \sin \frac{2\pi}{L} mx \sin \frac{\pi}{D} ny, \right.$$

$$\left. 2 \cos \frac{2\pi}{L} mx \sin \frac{\pi}{D} ny \right\},$$

$$m = 1, 2, ..., M, \qquad n = 1, 2, ..., N \tag{2.12}$$

as in CD. The functions G are orthonormal and satisfy the boundary conditions since

$$\frac{\partial G_i}{\partial x} = 0 \qquad \text{at} \quad y = 0, D, \tag{2.13a}$$

$$\frac{1}{L}\frac{1}{D} \int_x \int_y G_i G_j \, dy \, dx$$

$$= \delta_{ij} = \begin{cases} 1 & \text{if } i = j \\ 0 & \text{if } i \neq j. \end{cases} \tag{2.13b}$$

In addition, they are eigenfunctions of the Laplace operator, i.e.,

$$\nabla^2 G_i = -a_i^2 G_i. \tag{2.14}$$

To derive the spectral form of the model equations, we expand each of the horizontally varying fields as in (2.11), and substitute the expansion into (2.10). By then applying a Galerkin procedure, a set of nonlinear equations is obtained that can be written for an arbitrary i as

$$\frac{dx_i}{dt} = \frac{1}{a_i^2} \left\{ u^* \sum_{j=1}^{L} b_{ji}\left(\frac{f_0}{H} h_j - a_j^2 x_j\right) \right.$$

$$+ \sum_{j=1}^{L} \sum_{k=1}^{L} c_{ijk} x_j \left(\frac{f_0}{H} h_k - a_k^2 x_k\right)$$

$$\left. + \beta \sum_{j=1}^{L} b_{ji} x_j - \frac{1}{\tau} a_i^2 x_i \right\}. \tag{2.15}$$

The usual notation

$$b_{ji} = \frac{1}{L}\frac{1}{D} \int_x \int_y G_j \frac{\partial G_i}{\partial x} \, dy \, dx,$$

$$\tag{2.16}$$

$$c_{kij} = \frac{1}{L}\frac{1}{D} \int_x \int_y G_k J(G_i, G_j) \, dy \, dx,$$

was used. The resulting system is solved for its stationary solutions using a continuation algorithm, the pseudo-arclength method, as was done previously by Legras and Ghil (1985). This technique, based on the fact that the steady-state solutions to (2.10) form curves in phase space, allows to move along these curves and construct the full solution diagram. Once the equilibrium solutions are obtained, (2.15) can be integrated in time if information is required on the behaviour of the flow in the vicinity of the equilibrium solutions. The time integrations can reveal, for example, whether an unstable equilibrium solution leads to a flow that oscillates about that unstable state, or to a transition to another (stable) equilibrium state.

2.2. Choice for the truncation

To estimate the number of modes that should be retained in the spectral expansion of the horizontally varying terms, we ran some experiments and calculated the energy transfer as a diagnostic tool to estimate when a certain convergence in the
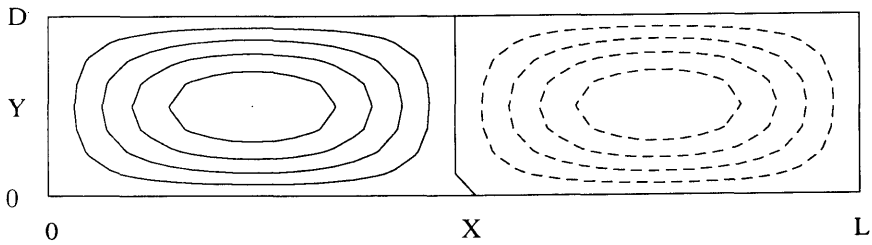
Fig. 1. The topography in the β-plane model. The contour interval is arbitrary.

behaviour of the solutions is reached. Through this method, we resolved to use a $(M, N) = (4, 5)$ truncation with a topography formed of wave $(m, n) = (1, 1)$ (see Fig. 1). We use a single wave topography since, as TR pointed out, the phenomenon of bent resonance can best be seen when there is only one Fourier mode of topographic forcing, and consequently, it is usually in this context that bent resonances are discussed.

3. Results from the β-plane model

In every case that we studied we have begun the integration along the solution curve using a quasi-linear approximation to the nonlinear solution. For the limits of large or small forcing (i.e., away from the linear resonance value), these approximations are fairly good and an exact solution is rapidly reached by applying a Newtonian scheme. The method used to obtain the quasi-linear approximation follows Pedlosky (1981); more details can be obtained from Gravel (1989).

It is difficult to choose a graphical representation (projection) for the solution curve that will be adequate for all the cases encountered. The intensity of the zonal wind $\bar{u}$ at mid-channel divided by the forced zonal wind u^* was adopted because of the easy physical interpretation it provides.

3.1. Solutions for a dissipation time constant of 11 days

The first series of results presented in Fig. 2 were obtained with a dissipation time constant of 11 days and topographic elevations of 500, 1000 and 1500 m. These values are chosen for their ability to generate interesting responses as far as multiple equilibria are concerned. Many arguments have been provided in the past to try to justify a particular choice for the damping time

scale or the topographic amplitude (TR, Charney et al., 1981) but in the present study these were not our primary concern.

To construct the solution curves, we applied the pseudo-arclength method to our system of equations by using u^*, the external forcing, as the key parameter, allowing it to vary between 10 and 35 m/s so as to include a reasonable range of the super- and subresonant values of the zonal wind. The linear resonance value of u^* for this numerical model is 24.3 m/s and is indicated in the figure by a full line.

The solutions along curve (a), corresponding to a mountain of 500 m, are all stable and depart only moderately from the state $\bar{u} = u^*$. The amplitude of the ϕ wave (not shown) reaches a maximum at the linear resonance value as is reflected by the minimum in the $\bar{u}/u^*$ curve. At the latter, the actual zonal wind at mid-channel is approximately 56% of the forced wind. In the flow pattern associated with this solution, the streamfunction ridge (not shown) is about 90 degrees west of the topographic ridge, maximizing the effect of the form-drag.

As the amplitude of the topography is increased to 1000 m, the boundary-forced interactions between the zonal and eddy components of the flow intensify, allowing stronger waves to be produced. As in curve (a), all the solutions are unique for all values of u^*, but there is now a loss of stability of the solution over part of the parameter range. As the value of u^* is increased from 20 to 21 m/s, a Hopf bifurcation occurs, followed by a second one between $u^* = 27$ and 28 m/s. Between these two values, the integration of the time-dependent model has yielded stable periodic solutions that remain very close to the low zonal index configuration of the stationary solution that they surround.

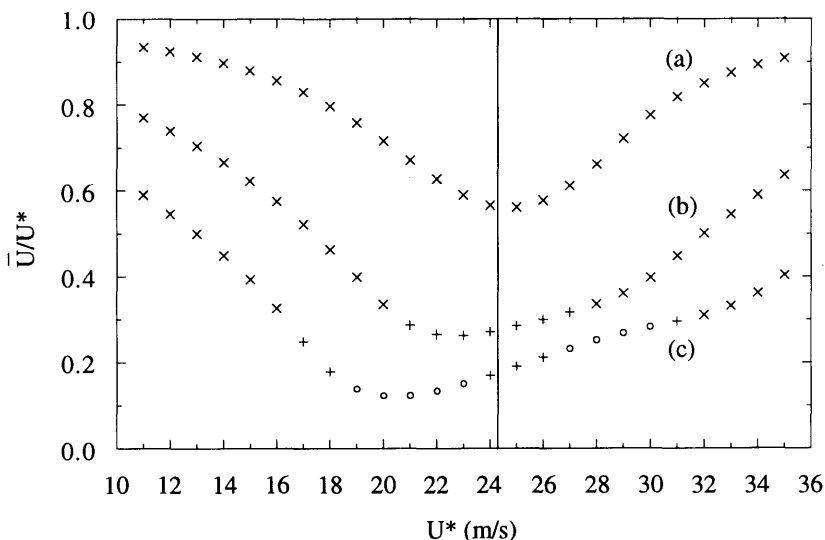For a topographic amplitude of 1500 m (Fig. 2

Fig. 2. $\bar{u}/u^*$ versus u^* for a dissipation time constant of 11 days and a topographic amplitude of (a) 500 m, (b) 1000 m, (c) 1500 m. The × symbol represents a stable solution whereas the other symbols indicate unstable solutions (eigenvalues with positive real part). A plus sign indicates the presence of two complex conjugate eigenvalues and a circle the presence of at least two pairs of complex conjugate eigenvalues.

curve (c)), an even stronger intensification of the waves due to increased boundary-forced inter-actions is noted, and consequently there is a substantial reduction of the intensity of the zonal wind accompanied by a distinct shift of the curve's minimum on the subresonant side of the linear resonance line. Another feature that distinguishes curve (c) from the preceding two is that now most of the stationary solutions are unstable. Between $u^* = 16.7$ and 16.8 m/s, a Hopf bifurcation occurs, quickly followed by a second one for u^* between 18.1 and 18.2 m/s and a third at u^* between 19.1 and 19.2 m/s. There are now 6 complex conjugate eigenmodes of the system that are unstable. The last pair of conjugate modes to become unstable regain their stability through another Hopf bifurcation for u^* between 22 and 22.1 m/s. The time-dependent model has been used to determine the evolution of flows initialized close to the equilibrium solution between the latter two bifurcations. For all values of u^* considered, periodic solutions surrounding the equilibrium flow were found. The trajectories are, however, relatively complex due to the higher harmonics of the fundamental frequency.

These results differ from those obtained by

Yoden (1985(a)). Using the same model as CD, he solved the set of 6 nonlinear equations resulting from the steady state potential vorticity equation. For a dissipation time constant of 11 days, he found the same three distinct stationary solutions as CD plus eight new steady state solutions resulting from pitchfork bifurcations and turning points along the new branches generated by the first. All the stationary solutions found by Yoden with this low-order model were also present in a high-order grid-point model. These results, of course, can be different from ours due to the use of a vorticity source in the CD model instead of a constant zonal wind forcing. They may also differ because of the very different geometry used by CD. As we recall, their β-plane channel measured 10,000 km in length and 5000 km in width.

3.2. Solutions for a dissipation time constant of 22 days

By reducing the damping time constant by a factor 2 we expect to see a more pronounced response of the wavy component of the flow in the vicinity of the linear resonance line. In Fig. 3, the solutions are presented in the same form as in Fig. 2 but for $\tau = 22$ days. As in the previous
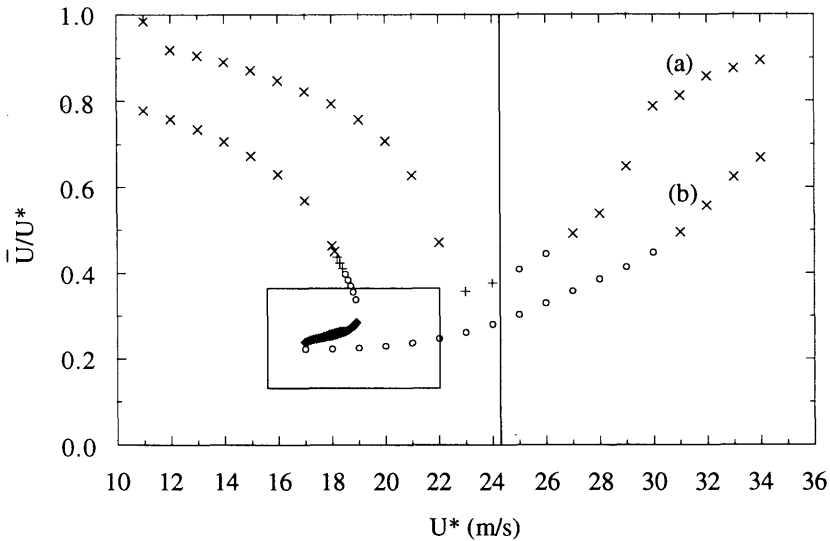
Fig. 3. $\bar{u}/u^*$ versus u^* for a dissipation time constant of 22 days and a topographic amplitude of (a) 500 m and (b) 1000 m. Stability symbols as in Fig. 2.

section, curves (a) and (b) correspond to topographic elevations of 500 and 1000 m, respectively.

When examining curve (a), it becomes obvious that the increase of the dissipation time constant has led to a much reduced zonal component. The wind $\bar{u}$ at mid-channel reaches a minimum of 36% of the forcing value at 23 m/s, on the subresonant side of u^*. Four Hopf bifurcations occur for $u^* = 22.3$, 24.9, 26.3 and 26.5 m/s. The unstable stationary solutions delimited by the first and last of these bifurcations are surrounded by stable periodic solutions, as verified by time-integrations of the model. For all values of u^* the solutions are unique.

When the amplitude of the topography is increased from 500 to 1000 m, the changes occurring in the pattern of the solution curve are substantial. Following the solution curve for increasing values of u^*, the solutions are at first unique and stable. For u^* between 18.1 and 18.2 m/s, a Hopf bifurcation occurs giving rise to unstable stationary solutions surrounded by periodic solutions. A second Hopf bifurcation occurs for u^* between 18.4 and 18.5 m/s. In Fig. 4, the stationary solution found for $u^* = 18.8$ m/s is shown together with snapshots of the stable periodic solution that surrounds it at different moments of its oscillation. As can be expected from the value of $\bar{u}/u^*$ corre-

sponding to this solution, we note that the streamline configurations are of a low index type.

At $u^* = 18.9$ m/s, there is a turning point and the amplitude of $\bar{u}/u^*$ now decreases for decreasing values of u^*. An enlarged view of the solution curve in this area is shown in Fig. 5. Following the curve, at $u^* = 18.4$ m/s, there is a pitch fork bifurcation. Of the two new branches appearing past this bifurcation, only one is visible in the figure, as this is a typical case where the projection chosen to illustrate the solution curve is inadequate. What distinguishes the two new branches of solutions is the sign of the coefficients of the $\bar{u}$ modes that are antisymmetric with respect to mid-channel and, therefore, do not contribute to the value of $\bar{u}$ at mid-channel. The new branches of solutions end at $u^* = 17.4$ m/s through a second pitchfork bifurcation. The solution curve, once again unique, goes through a second turning point at $u^* = 17.0$ m/s. Between the two turning points the solutions are all unstable, as we can tell from the presence of at least one purely real eigenvalue. Past the second turning point at $u^* = 17.0$ m/s the solutions with the lowest zonal index are also unstable but only complex conjugate eigenvalues with a positive real part are found, indicating the possible presence of periodic solutions.

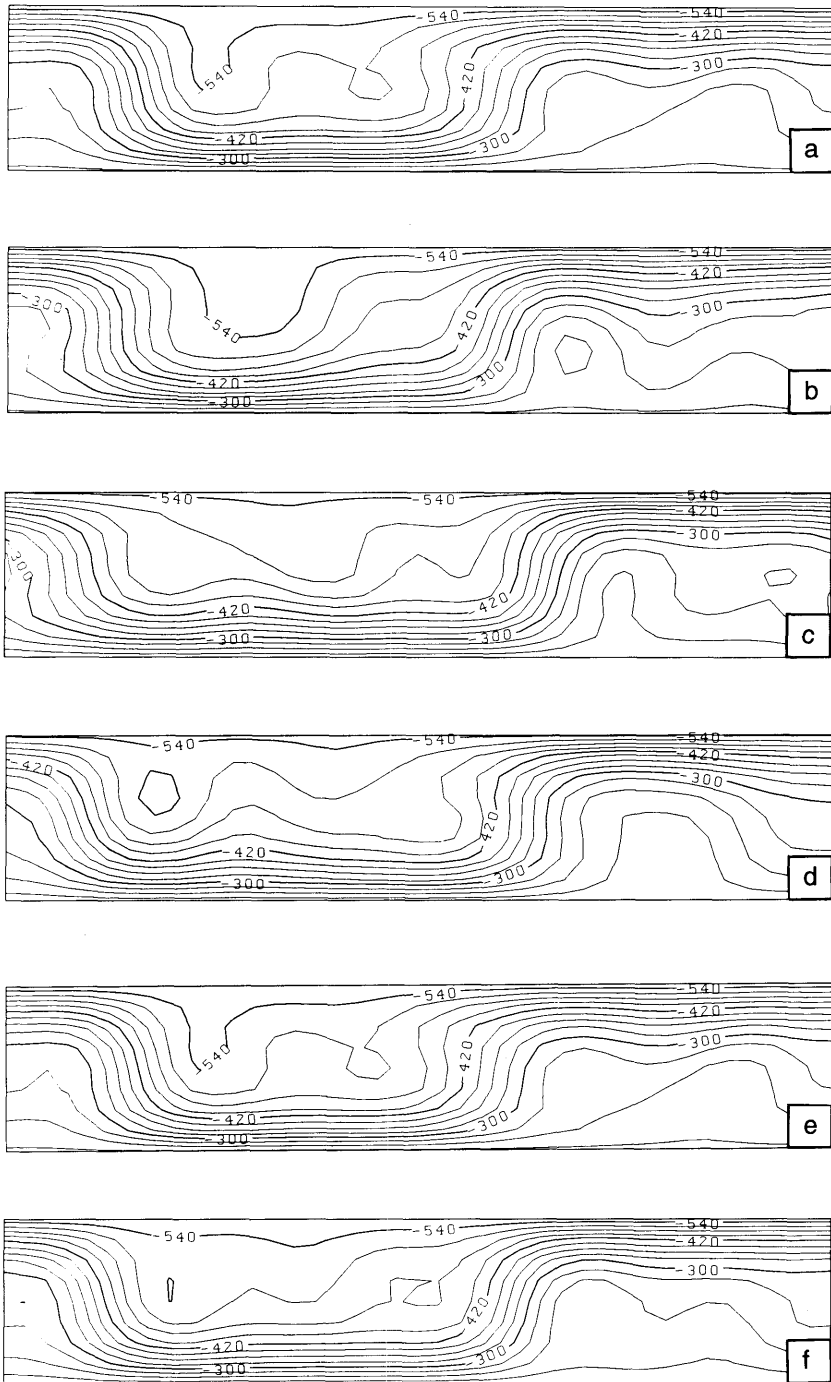If we now consider all possible branches of solu-

Fig. 4. Streamlines of the solutions for $\tau = 22$ days, $h_0 = 1000$ m and $u^* = 18.8$ m/s; (a) unstable steady solution, (b)–(f), stable periodic solution at different moments of its period. Units: 1×10^{-5} m²/s.
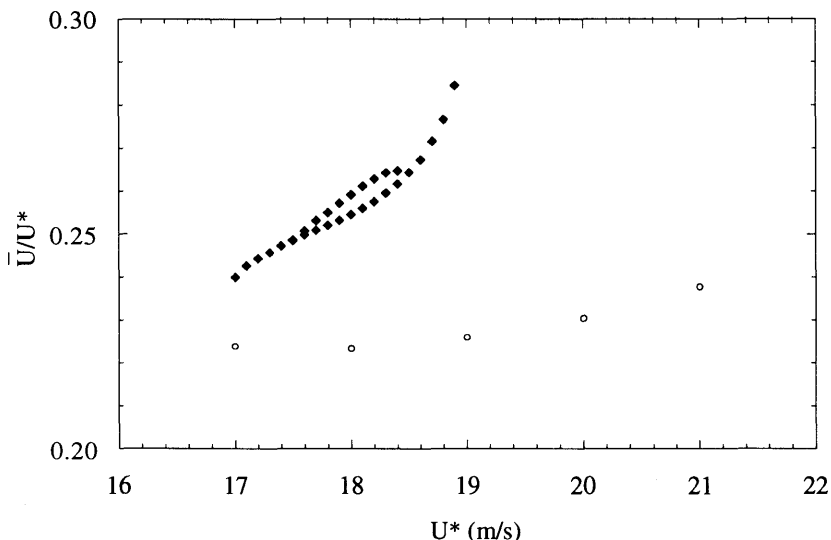
Fig. 5. As in Fig. 3, curve (b). The black squares indicate the presence of at least two eigenvalues, at least one of which is real and positive; circles as in Fig. 2.

tions, we find that for the values of u^* between 17 and 18.9 m/s there are three, sometimes as many as five distinct equilibrium solutions to the vorticity equation. Fig. 6 shows the streamlines of the equilibrium solutions present at $u^* = 17.8$ m/s. All solutions, except the one shown in Fig. 6a which corresponds to the upper solution branch in Fig. 3, curve (b), are unstable. Because it lies on the upper solution branch, with a larger value of $\bar{u}/u^*$, the stable solution presents a structure with a higher zonal index than the remaining ones. These results could suggest the presence of multiple equilibria for this range of values of u^*. Time integrations, however, have indicated the contrary. When the solutions with the lowest zonal index, which we have already found to be unstable due to the presence of at least one pair of unstable complex conjugate eigenmodes, are slightly perturbed, their evolution in time does not lead to the emergence of periodic solution that can be linked to the unstable stationary solution. In Figs. 7a, b, the time series of the amplitude of the gravest zonal mode is plotted for the lowest zonal index solutions at $u^* = 17.2$ and 18.5 m/s. In both cases, the solution slowly evolves away from the stationary state, comes under the influence of the solution with the highest zonal index and is captured. In one case

(Fig. 7a), this solution is stationary and stable. In the second case it is periodic and stable. In short, while multiple equilibrium solutions exist between $u^* = 17.0$ m/s and 18.9 m/s (Fig. 3, curve (b)), only the upper branch has solutions that are stable or periodic. The solutions on the branches with lower values of $\bar{u}/u^*$ are unstable and will not be observed over extended periods of time.

The above solution characteristics will undoubtedly lead to an hysteresis transition between the lower and upper branches of the solution curve. Indeed, as the value of u^* is decreased past the critical value of $u^* = 18.9$ m/s, the solution will "jump" from the lowest to the upper branch. As we recall, the solutions are periodic in both cases and the difference in zonal index between the unique solution found at $u^* = 19.0$ m/s and the solution on the upper branch for $u^* = 18.9$ m/s (Fig. 3) is so small that the hysteresis jump is likely to go unnoticed by an observer.

In summary, for a dissipation time constant of 22 days and a topographic amplitude of 1000 m, stable solutions (either periodic or stationary) do not coexist. In the presence of multiple solutions to the steady state potential vorticity equation, only one can be observed in a time integration model. These results are very different from those
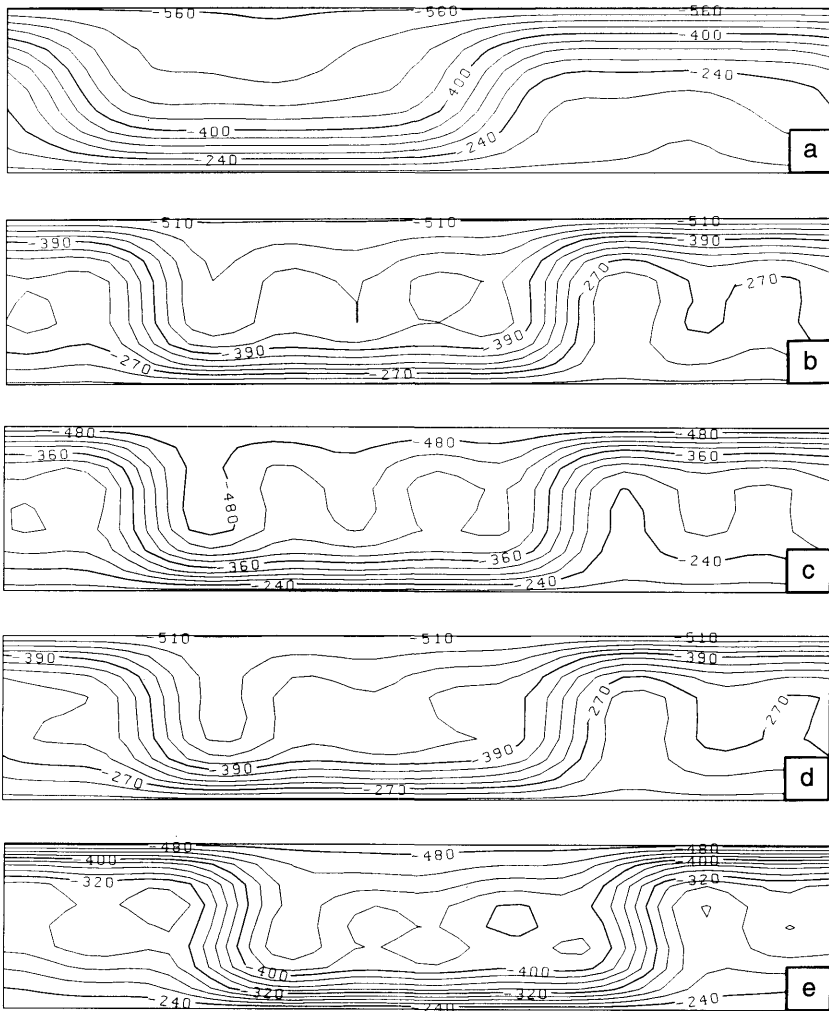
Fig. 6. Streamlines of the solutions for $\tau = 22$ days, $h_0 = 1000$ m and $u^* = 17.8$ m/s; (a) stable steady solution on the upper branch of curve (b), Fig. 3; (b)–(e), unstable steady solutions on the lower branches of the same curve. Units: 1×10^{-5} m^2/s.

obtained by Yoden (1985a) with his model. The comparison can only be qualitative, however, since our model and his only share a common topographical amplitude, in contrast to the forcing, dissipation and geometry of the channel which are different in the two studies.

3.3. Dependence of the solutions on the geometry

Using dimensional analysis, Rambaldi and Mo (1984) have studied the importance of the meridional scale of the topography by examining the solutions in the limits of extremely wide and extremely narrow channels. They have shown that in the first case the wave-wave interactions vanish and wave-topography interactions are relevant only to the evolution of the zonal flow. In the limit as the channel width tends to zero, the wave-wave and wave-topography interactions vanish. They emphasized the interest, therefore, of studying problems where the meridional and zonal wavelengths of the topography are of comparable magnitude.
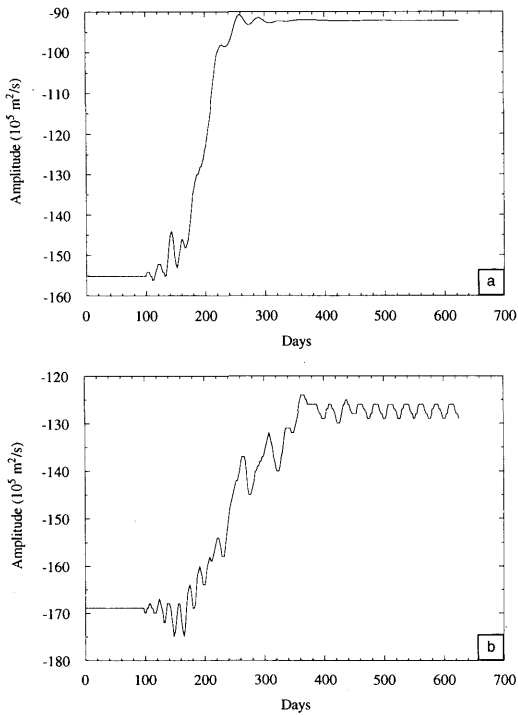
Fig. 7. Time series for the amplitudes of the gravest mode (a) $u^* = 17.2$ m/s, (b) $u^* = 18.5$ m/s. Units: 10^5 m^2/s.

Holloway and Eert (1987) have shown, using a higher resolution model, that it is possible to observe intransitive multiple equilibria over a range of parameter values. In particular, they showed results with evidence of multiple equilibria on the superresonant side of the linear resonance line when the various parameter values are fixed to $h_0 = 629$ m, $\tau = 8.7$ days and the zonal forcing $u^* = 13.3$ m/s. The major difference between our numerical model and theirs, besides their inclusion of a higher order friction that selectively damps small scale vorticity, is their choice of the model geometry. The latter is doubly periodic, with a fundamental length and width of 6000 km. We have found, through experiments, that the impact of the double periodicity on the multiple equilibria is negligible. The width of the channel, however, has a much stronger impact. In Fig. 8 are shown results that were obtained for channels with three different widths. Curves (a), (b) and (c) correspond to widths D of 2000, 4000 and 6000 km, respectively. For each geometry, the
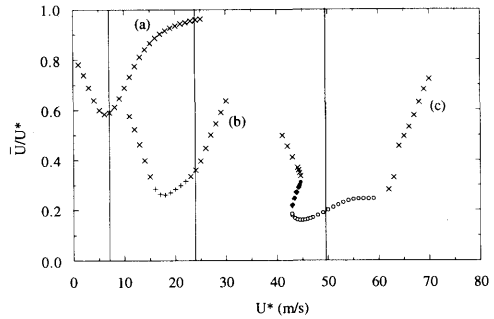

Fig. 8. $\bar{u}/u^*$ versus u^* for a dissipation time constant of 11 days, a topographic amplitude of 1000 m, and a channel width of (a) 2000 km, (b) 4000 km and (c) 6000 km. The black dot represents the presence of one real positive eigenvalue (unstable); the other symbols are as in Figs. 2 and 5.

linear resonance line (given by $u^* = \beta/K^2$, where K is the two-dimensional wavenumber) is indicated. As the value of D is increased, we note a stronger response of the eddy component of the flow, and a tendency for the position of the resonant peak to shift to the subresonant side of the linear resonance line. The curve for the widest channel even exhibits a fold that indicates the presence of multiple solutions, and potentially multiple equilibria. This behaviour suggests that the differences between our results and those obtained by Yoden can also be a reflection of the major differences between the two geometries used. The discrepancies between these results have suggested the use a hemispheric model, in which, of course, the width of the channel need not be specified arbitrarily. In Sections 4 and 5, we will turn to the formulation and use of such a model.

4. The hemispheric model

To ease comparison between our β-plane and hemispheric models we will try to limit the difference between them to a minimum, at least in the linear versions of the models, by appropriate choices for the zonal momentum forcing, the topography and the dissipation time scale.

While the formulation of the potential vorticity equation is unchanged by the passage to spherical geometry, the potential vorticity, q, on the other hand, must be redefined to take into account the

variation of the Coriolis parameter on the sphere, and is now given by:

$$q = \nabla^2 \psi + f\left(1 + \frac{h_0}{H}\right), \qquad (4.1)$$

with

$$f = 2\Omega \sin \theta. \qquad (4.2)$$

As is commonly done, surface harmonics Y_n^m will be used as basis functions for the spectral expansion so

$$\psi = \sum_k \psi_k Y_k, \qquad (4.3)$$

where k represents a couple (n, m) and

$$Y_k = e^{im\lambda} P_n^m(\mu), \qquad (4.4)$$

with λ and μ, the longitude and the sine of the latitude, respectively and P_n^m, the associated Legendre polynomial of the first kind. We will use a hemispheric model, so that only the modes with $(n - m)$ odd are retained in the representation of ψ, and due to the reality condition,

$$\psi_n^{-m} = (-1)^m \left[\psi_n^m\right]^*, \qquad (4.5)$$

so that only the coefficients for $m \geqslant 0$ need be calculated. Applying the spectral expansion to the governing equation, the equivalent for the hemispheric model of (2.15) takes the form

$$\frac{\partial \psi_k}{\partial t} = \frac{r^2}{n(n+1)} \left[\sum_i \sum_j a_{kij} \left[\widetilde{\mu h_j} - \frac{n_j(n_j+1)}{r^2} \psi_j \right] \psi_i \right.$$
$$\left. + \frac{2 im\Omega}{r^2} + \frac{1}{\tau} \frac{n(n+1)}{r^2} (\psi_k^F - \psi_k) \right], \qquad (4.6)$$

where r is the radius of the Earth, a_{kij} are the interaction coefficients and $\widetilde{\mu h_j}$ are the spectral coefficients of the effective topography of the model, resulting from the product of the Coriolis parameter and h_0/H. The effective topographic structure is formed of only one mode, Y_4^3, and has the structure illustrated in Fig. 9. With this particular choice, the non-dimensional wavenumber of the topography in the two models, the β-plane and the hemispheric, is comparable, i.e., $6.66 \times 10^{-13} \, \text{m}^{-2}$ and $4.93 \times 10^{-13} \, \text{m}^{-2}$, respectively. The hemispheric equivalent to the forcing
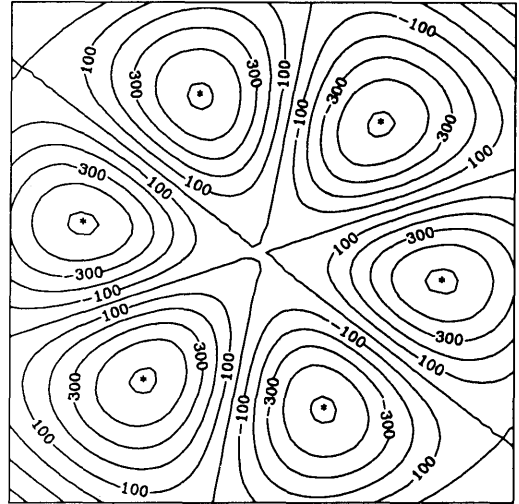

Fig. 9. Structure of the topography in the hemispheric model. The contour interval is arbitrary.

used in the β-plane model is a zonal flow with constant angular velocity and therefore, in terms of the streamfunction, it is simply

$$\psi^F = -\kappa Y_1^0, \qquad (4.7)$$

where κ is a constant. The superscript F is used to indicate the forcing instead of an asterisk to avoid confusion with the complex conjugate coefficients.

A triangular truncation is used, i.e., one where $0 \leqslant n \leqslant N$ and $-n \leqslant m \leqslant n$. After testing for convergence in behaviour, the choice of a T9, i.e., $N = 9$, was adopted.

Our choice of the dissipation time constant is guided by a consideration of the linearized vorticity equation. By inspection of that equation it is seen that two models having a topographic forcing with the same two-dimensional wavenumber and same amplitude will have the same response amplitude provided τk is the same in both model, where k is the zonal wavenumber. As the zonal wavenumber is about $3 \times$ larger in our hemispheric model as compared to our β-plane model, the value of τ should be decreased by a factor of about 3. It should be noted that the above arguments apply only to the linear versions of the models. As will be seen, our β-plane and hemispheric models have different nonlinear responses to the topographic forcing, as could be expected, in particular, from the fact that the ratio

of the zonal to the meridional dimensions of the orography is not the same in both models. In fact, the differences in the results of the two models will highlight the sensitivity of the nonlinear effects to the geometry of the orographic forcing.

5. Results from the hemispheric model

5.1. Solutions for a dissipation time constant of 3.2. days

The results shown in Fig. 10 were obtained with the strongest dissipation used in the hemispheric model, i.e., a dissipation time constant of 3.2 days. Three curves for $\bar{u}/u^*$ versus u^* corresponding to three different topographic amplitudes, (a) 650 m, (b) 1000 m and (c) 1500 m, are presented. Here again, in order to ease the comparison with the β-plane model, the forcing ψ^F is translated into the intensity of the forced zonal wind u^* at 60° of latitude, which ranges from 10 to 80 m/s. The vertical axis shows the ratio of the actual zonal wind $\bar{u}$ to u^* when both are evaluated at 60°. The first two curves in Fig. 10 suggest the development of a *bent resonance* to the right of the resonance line (indicated on the figure by a vertical line) as the topographic amplitude increases. We recall that in the β-plane model the multiplicity of solutions was on the subresonant side.

For a topographic amplitude of 650 m (Fig. 10, curve (a)), there is a unique stable solution for a given u^*. The maximum amplitude for the wavy part of the flow is reached on the superresonant side of the critical line at a corresponding forcing wind of 31 m/s. In general the solutions do not depart significantly from the forcing flow, the minimum for $\bar{u}/u^*$ being only of 0.75. When the topographic amplitude is increased to $h = 1000$ m, the bending of the resonant curve becomes sufficiently important to form a fold in the curve. In terms of bifurcations, we are in presence of two turning points at $u^* = 38$, and 37.2 m/s. For this narrow range of values of u^* there are three distinct steady state solutions, *two of which are stable* and one is unstable. The stable solutions, as is obvious from Fig. 11(a, b), belong to two distinct regimes, a high and a low zonal index, while the unstable solution (Fig. 11c) has an intermediate structure.

As we further increase h to 1500 m (Fig. 10, curve (c)), the fold in the solution curve becomes slightly more pronounced and the turning points are now at $u^* = 44.1$ and 42.0 m/s. There are also two new features, namely, the presence of two Hopf bifurcations and a new minimum in the solution curve at $u^* = 27.9$ m/s. The first new bifurcation occurs at $u^* = 43.7$ m/s and the unstable complex eigenmodes regain their stability at
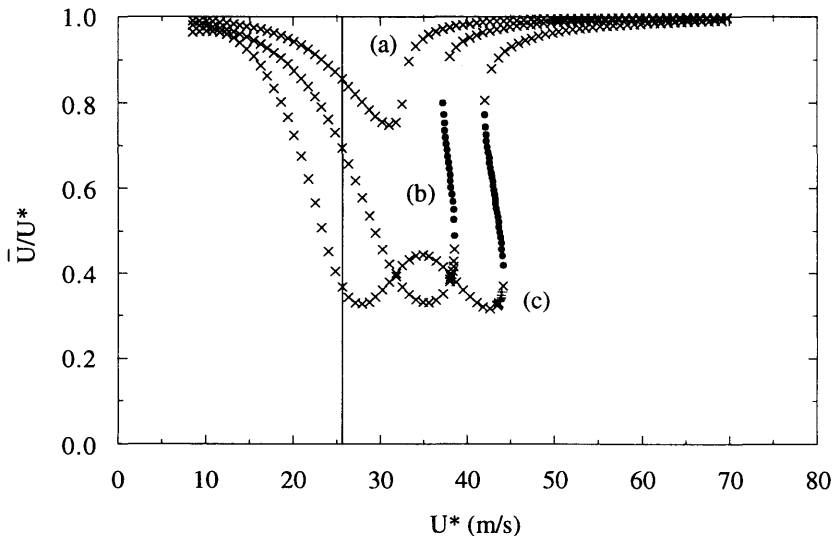

Fig. 10. $\bar{u}/u^*$ versus u^* evaluated at 60°, for a dissipation time constant of 3.2 days and a topographic amplitude of (a) 650 m, (b) 1000 m, (c) 1500 m. Stability symbols as in Figs. 2 and 8.
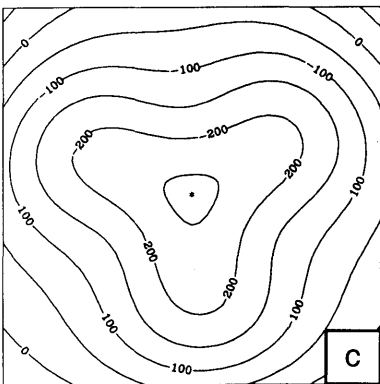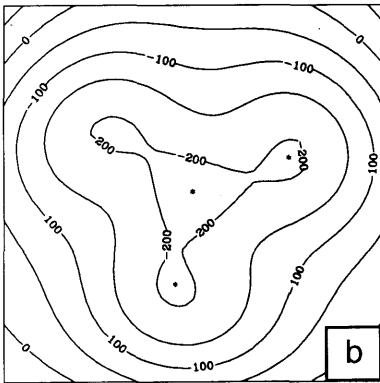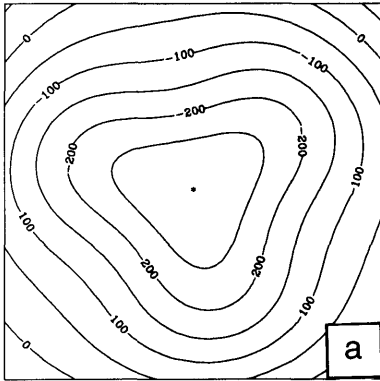
Fig. 11. Streamlines of the solutions for $\tau = 3.2$ days, $h_0 = 1000$ m and $u^* = 37.6$ m/s; (a) and (b) stable steady solutions corresponding to the highest and lowest branches of curve (b) in Fig. 10, and (c) unstable steady solution corresponding to the intermediate branch. Units: 1×10^{-6} m^2/s.

the second Hopf bifurcation, at $u^* = 44.1$ m/s. The steady state solutions between these two values are unstable but are surrounded by stable periodic solutions that remain very close to the steady state unstable solution that they surround. This behaviour was observed in integrations of the time-dependent version of the model.

In summary, we have found that for both $h = 1000$ m and 1500 m, two distinct stable flow regimes exist for a range of u^*. That range of u^*, however, is quite narrow.

The occurrence of a second minimum in curve (c) of Fig. 10 is reminiscent of the results of Legras and Ghil (1985) who observed as many as four minima. The multiplicity of resonant peaks in their study can easily be explained through linear resonance. Indeed, the forcing used by Legras and Ghil is formed of the two modes: Y_1^0 and Y_3^0. It is the interaction of the latter with the modes having the same zonal wavenumber as the topography that generates the multiplicity of peaks. A linear resonance analysis shows that a zonal forcing formed only of Y_1^0 (as in the present study) will lead to resonance only in the topographic modes, independently of the meridional resolution of the model. The second peak in curve (c) of Fig. 10 must therefore be due to the nonlinearities of the model.

To pursue the parallel between the work of Legras and Ghil and ours we need to recall that for their numerical integration, they used as key parameter the non-dimensional factor ρ, where

$$\rho = \frac{U}{2\Omega r}, \qquad (5.1)$$

and U is the characteristic speed. ρ measures the intensity of the forcing since the dimensional and non-dimensional forcing (indicated by a subscript d) are linked by the relation

$$\psi^F = \rho U \psi_d^F. \qquad (5.2)$$

In terms of ρ, the range of values of u^* we have examined (10–80 m/s) corresponds roughly to $\rho = 0.30$ to 0.33. Because of their choice of zonal structure for the topography (zonal wavenumber 2), the domain Legras and Ghil needed to study in order properly to analyze the nonlinear behaviour of their solutions is much wider and the position of their resonance peak is of course different from

ours. It is important to note that for a dissipation time of 3.3 days and a topographic amplitude of 1000 m, the solutions obtained by Legras and Ghil are always stable and stationary. The most likely cause of the difference between their results and ours is linked to the sensitivity of the nonlinear terms to the topographic structure, which is different in the two studies.

If we now compare our hemispheric results with those obtained with the β-plane model, we can find some similarities, but also some notable differences. In Fig. 10, the minimum of each of the curves occurs for values of $\bar{u}/u^*$ similar to those in Fig. 2. Besides the values of the minima, the other similar feature is the presence of Hopf bifurcations on both curves (c). In general, however, the configuration of the curves is very different for the two geometries. While in the hemispheric model the nonlinear response in the neighborhood of the resonance line is very sharp, i.e., occurring in a narrow band, the β-plane model has a much broader response. This is particularly obvious when the slopes of the solution curves on either side of the resonance peak are compared. The evolution of the curves as the amplitude of the topography is increased is also different. In the β-plane model the curves undergo a global translation toward lower values of $\bar{u}/u^*$, whereas in the hemispheric model the tilting of the tangent to the curve is the most notable feature.

5.2. Solutions for a dissipation time constant of 5.6 days

It seems reasonable to expect that the qualitative effects of the reduction of the dissipation are independent of the geometry of the model, and therefore, as for the β-plane model, the reduction of the damping should lead to a more pronounced response of the wavy component of the flow. Fig. 12 is the same form of representation as Fig. 10, but for $\tau = 5.6$ days, and the results for only the lowest two amplitudes of the topograpy are examined.

For a topographic height of 650 m (Fig. 12, curve (a)), there are now 2 turning points at $u^* = 38.4$ and 34.6 m/s, bounding a fold in the solution curve. Over this range of values of u^* there are 3 distinct solutions, with the one corresponding to the intermediate value of $\bar{u}/u^*$ being unstable.

When the amplitude of the topography is

increased to 1000 m (Fig. 12, curve (b)), the resulting solution curve resembles the one observed in Fig. 10, curve (c). It has 2 minima and the first, occurring at $u^* = 27.1$ m/s, seems to be related to the quasi-resonance of the same mode as in Fig. 10, curve (c). The second minimum corresponds to the growth of the topographically forced mode. Along the solution curve, 12 bifurcations are encountered, 2 of which are turning points occurring at $u^* = 42.3$ and 38.2 m/s. The remaining bifurcations are Hopf bifurcations giving rise to stable periodic solutions.

Obviously, the difference between the β-plane and the hemispheric models persist when the dissipation time constant is increased to 5.6 days. In the hemispheric model, the pitchfork bifurcations are absent. The conditions that lead to their emergence in the β-plane model were described by Yoden (1985a, b), who divided the basis functions ϕ of his numerical model into two symmetry groups. By considering the transformation T:

$$T: Z(x, y) \rightarrow -Z(x + \pi/2, \pi - y), \qquad (5.3)$$

for a cyclic channel of dimension π in x with lateral walls at $y = 0$ and π, he divided the spectral components according to their variance to T^n. He obtained two groups which he labeled the S modes and the T modes defined by

$$\begin{aligned} \text{S modes}: \phi &= T(\phi) \\ \text{T modes}: \phi &= -T(\phi) = T^2(\phi). \end{aligned} \qquad (5.4)$$

Since the forcings, external and topographic, belong to the same symmetry group, the free modes of the other symmetry group, when initially set to zero, remained zero. The branching observed by Yoden and by us always corresponds to the change of stability of an eigenmode formed of a linear combination of these unforced modes. In the hemispheric model, the distinction between two symmetry groups is difficult to make because of the absence of latitudinal symmetry in the structure of the associated Legendre polynomials. However, with our particular choice of external and topographic forcing, the non-linear interactions do not excite some of the modes if they are initially set to zero. These modes belong to the free group but never go through a pitchfork bifurcation. The numerical model used by Legras and Ghil, with a similar number of degrees of freedom but with
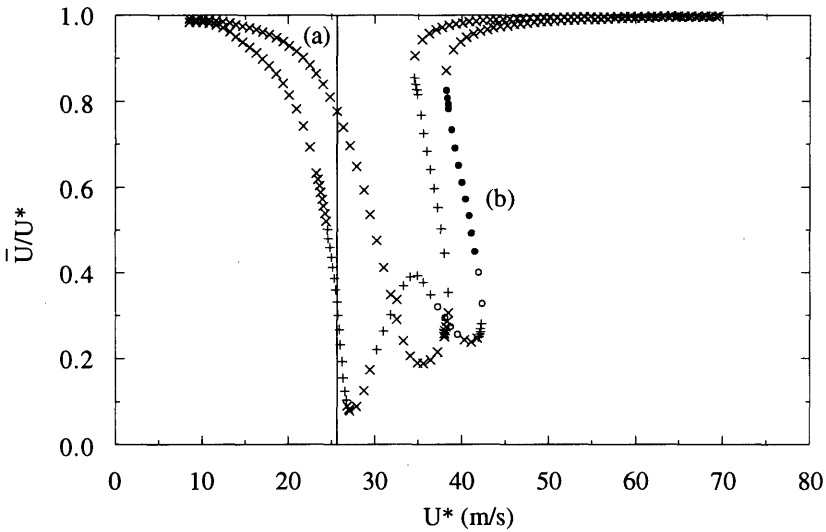
Fig. 12. As in Fig. 10 but for a dissipation time constant of 5.6 days and a topographic amplitude of (a) 650 m and (b) 1000 m.

different modes being included, does not show the presence of branching either. The pitchfork bifurcations thus seem to remain an exclusive feature of the β-plane model.

In the next section, we will further increase the dissipation time constant to 8 days, and we will complete the analysis of the solution curve by looking in detail at the limit cycles associated with the low index solutions.

5.3. Solutions for a dissipation time constant of 8 days

The results obtained with a dissipation time constant of 8 days and a topographic amplitude of 650 m are illustrated in Fig. 13 using the usual projection. The solution curve has evolved with the decrease in dissipation in the way we have come to expect. The fold in the solution is now more pronounced, the 2 limiting turning points occur-
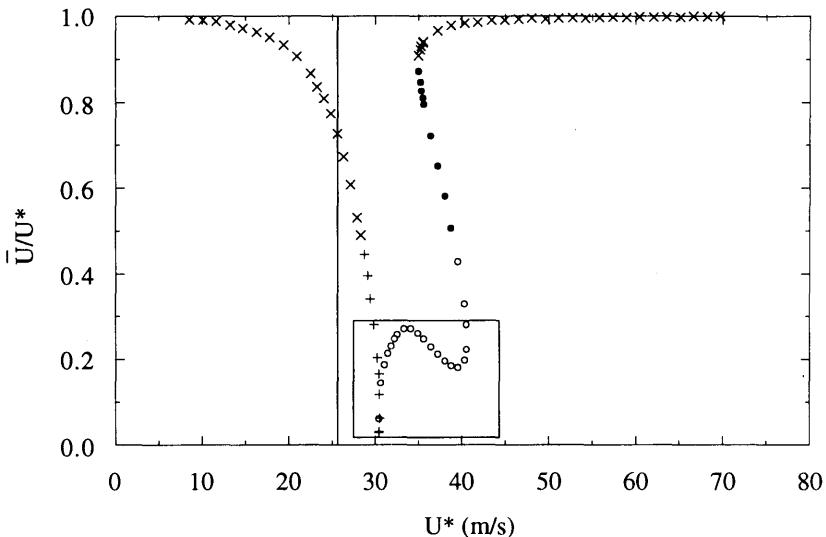

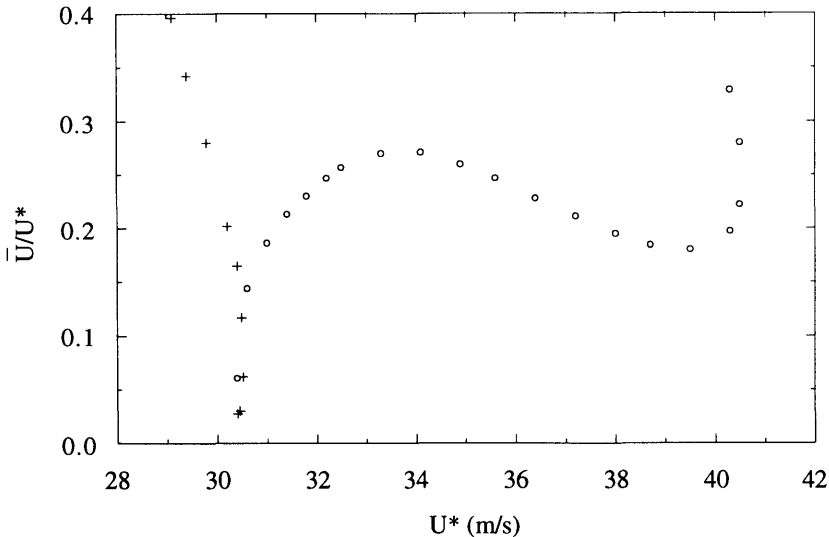*Fig. 13.* As in Fig. 10 but for a dissipation time constant of 8 days and a topographic amplitude of 650 m.

Fig. 14. An enlarged segment of Fig. 13.

ring for values of $u^* = 35.0$ and 40.5 m/s so that for a moderate range of 5.5 m/s there are multiple equilibria. It is important to note, however, that both the intermediate and the low index solutions are unstable. It should be noted however that the latter give rise to stable periodic solutions for the values of u^* between 35.0 and 40.2 m/s.

The secondary minimum observed in Fig. 10, curve (c) and Fig. 12, curve (b) is also present here. An enlarged view in the area of this minimum is shown in Fig. 14. The curve has a γ shape whose width is delimited by two turning points occurring at $u^* = 30.5$ and 30.4 m/s. Over this narrow range three solutions coexist, all with nearly the same zonal index, and therefore not giving rise to multiple regimes.

We come across four Hopf bifurcations in Fig. 13 as we move along the solution curve for increasing values of u^*. The first occurs at $u^* = 28.6$ m/s. The pair of complex conjugate eigenmodes that becomes unstable at this point regains its stability at what we refer to as the third Hopf bifurcation, at $u^* = 39.5$ m/s. The second Hopf bifurcation is at $u^* = 30.4$ m/s and the associated complex eigenmodes regain their stability just past the first turning point for $u^* = 40.35$ m/s, i.e., at the fourth Hopf bifurcation. So for the values of u^* between 30.4 and 39.5 m/s, there are 2 pairs of unstable complex conjugate eigenmodes.

Legras and Ghil (1985) have paid particular attention to the results obtained for a dissipation time constant of 20 days and an external forcing of approximately 60 m/s at 50° of latitude. They observed a chaotic behaviour that led to a succession in time of different planetary flow regimes. Since chaos occurs through the degeneracy of periodic solutions via period doubling, we used the time-dependent model to examine the behaviour of the unstable solutions for the values of u^* between 30.4 and 39.5 m/s. Aperiodic regimes were found to occur for values of u^* greater than 36.5 m/s, but they are characterized by low index configurations, that is, by the absence of transitions from one regime to another.

An interesting transition phenomenon between low and high index solutions was observed, however, for the unstable low index steady state solution present for $u^* = 40.3$ m/s. When the latter is perturbed and allowed to evolve in time, the unstable eigenmode that originally has zero amplitude starts to grow. In the process, it brings the solution under the influence of the attractor basin of the high index stationary solution (top branch in Fig. 13). The solution is then captured, and the unstable eigenmode recovers its null amplitude. This phenomenon is illustrated in Fig. 15, where in (a) it can be seen that the unstable eigenmode is growing as a result of the
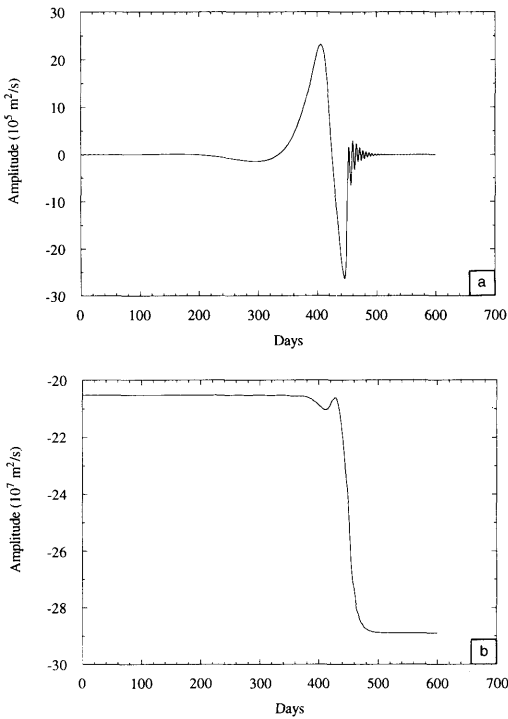
Fig. 15. Time evolution for $u^* = 40.3$ m/s of (a) the amplitude of the real part of the unstable eigenmode in units of 10^5 m^2/s; (b) the amplitude of Y_1^0 in units of 10^7 m^2/s.

perturbation added to the stationary solution. As it grows, however, it is captured by the other stationary solution present for this value of u^*. Since the eigenmode has a zero amplitude for that solution, we have chosen to illustrate this phenomenon in a different fashion, by plotting this time the evolution of the amplitude of Y_1^0 over the same time period (Fig. 15b). This particular mode was chosen because the absolute value of its amplitude is proportional to the intensity of the zonal wind of the corresponding solution and, therefore, illustrates well that the solution moves from a low index to a high index structure. This result implies that the attractor basins for the high and low index solutions have merged and there is only one observable equilibrium, namely the stable stationary solution. Thus a transition from a low index to a high index solution can occur for small changes in the value of the parameter u^*. In the case shown, the transition occurs on a time scale of approximately 40 days.

6. Summary and conclusions

A barotropic β-plane model was used to examine the equilibrium flows that result when a zonal current is forced in the presence of orography. For sufficiently weak dissipation, multiple equilibrium solutions were found, but only one of them, with a relatively high zonal index, was stable. Time integrations of the model started close to the other (unstable) solutions with a lower zonal index showed that the flow does not reach a limit cycle, but rather evolves away from the initial conditions towards the high index stable solution. In other words, while there are formally more than one equilibrium solutions, only one of them could be observed in a time dependent model.

In the vicinity of the linear resonance point, only one, unstable, solution was obtained for a given forcing amplitude. In that region of parameter space the nature of the nonlinearities are such that flows started close to the unstable equilibrium states first move away from the equilibrium state, but then reach a limit cycle close to the equilibrium solution. The flow thus oscillates in a periodic fashion about the equilibrium. In spite of its instability, the equilibrium solution can in this case be recovered from a suitable time averaging of the time-dependent flow.

Experiments conducted with different β-plane channel widths revealed that the results are quite sensitive to the meridional scale of the topography and further calculations were made with a spherical geometry model. The two-dimensional wave number of the topography in the spherical geometry model was chosen to be the same as for the β-plane model, and the dissipation time constant was adjusted so that both models produced linear solutions of similar amplitudes for similar mid-latitude zonal flows. The spherical geometry nonlinear model produced a bent resonance with multiple equilibria, two of which were stable, but only over a very small range of zonal flow driving amplitudes. When the dissipation time constant was increased from 3.2 to 8 days, multiple equilibria were observed for realistic forcing amplitudes. The range of mean zonal flow forcing amplitudes over which multiple equilibria are found is, on the other hand, rather modest.

The differences in the results obtained with the β-plane and the spherical geometry model highlight the sensitivity of the nonlinearities to the

geometry of the forcing. While both models used parameters adapted to yield comparable linear solutions, the ratio of the zonal to the meridional dimensions of the topography was different in the 2 models. While different in many ways, the results obtained with both models indicate that rather special circumstances must be met for multiple equilibria to exit. In addition, the sensitivity of the results to the geometry of the topography suggests that it is difficult to draw general conclusions on the existence of multiple equilibria in more general models and in the atmosphere.

The study has provided interesting examples of equilibrium solutions which, while unstable to infinitesimal perturbations, were stable in the nonlinear sense in that the flow oscillated around the unstable equilibria.

7. Acknowledgments

REFERENCES

Charney, J. G. and DeVore, J. G. 1979. Multiple flow equilibria in the atmosphere and blocking. *J. Atmos. Sci. 36*, 1205–1216.

Charney, J. G., Shukla, J. and Mo, K. C. 1981. Comparison of a barotropic blocking theory with observation. *J. Atmos. Sci. 38*, 762–779.

Gravel, S. 1989. *Periodic and stationary solutions to a forced-dissipated barotropic model of the atmosphere.* Available as CRG Report #89-3, Department of Atmospheric and Oceanic Sciences, McGill University, 116 pp.

Holloway, G. and Eert, J. 1987. Intransitive multiple equilibria in eddy-active barotropic flows. *J. Atmos. Sci. 44*, 2001–2005.

Källén, E. 1982. Bifurcation properties of quasi-geostrophic, barotropic models and their relation to atmospheric blocking. *Tellus 34*, 255–265.

Keller, H. B. 1978. Global homotopies and Newton methods. *Nonlinear analysis*, (Eds., C. de Boor and G. H. Golub), Academic Press, 73–94.

Legras, B. and Ghil, M. 1985. Persistent anomalies, blocking and variations in atmospheric predictability. *J. Atmos. Sci. 42*, 433–471.

Pedlosky, J. 1981. Resonant topographic waves in barotropic and baroclinic flows. *J. Atmos. Sci. 38*, 2626–2641.

Rambaldi, S. and Mo, K. C. 1984. Forced stationary solutions in a barotropic channel: Multiple equilibria and theory of nonlinear resonance. *J. Atmos. Sci. 41*, 3135–3146.

Tung, K. K. and Rosenthal, A. J. 1985. Theories of multiple equilibria. A critical reexamination. Part I: Barotropic models. *J. Atmos. Sci. 42*, 2804–2819.

Yoden, S. 1985a. Bifurcation properties of a quasi-geostrophic, barotropic, low-order model with topography. *J. Meteor. Soc. Japan 63*, 535–546.

Yoden, S. 1985b. Multiple stable states of quasi-geostrophic barotropic flow over sinusoidal topography. *J. Meteor. Soc. Japan 63*, 1031–1045.

Wiin-Nielsen, A. 1979. Steady states and stability properties of a low order barotropic system with forcing and dissipation. *Tellus 31*, 375–386.